NUMERICAL SIMULATION OF FLUID FORCE ACTING ON CIRCULAR CYLINDERS IN UNIDIRECTIONAL FLOW

Sota Nakajo
Disaster Prevention Research Institute
Kyoto University
Gokasho, Uji, Kyoto, 611-0011 Japan
nakajo@oceanwave.jp

Yusuke Takeoka
Graduate school of Engineering
Osaka City University
3-3-138 Sugimoto, Sumiyoshi-ku, Osaka, 558-8585 Japan
y.takeoka13@gmail.com

Takaaki Shigematsu
Graduate school of Engineering
Osaka City University
3-3-138 Sugimoto, Sumiyoshi-ku, Osaka, 558-8585 Japan
shige@urban.eng.osaka-cu.ac.jp

ABSTRACT

There is few research on turbulent flow in a pore of porous media and fluid force acting on its components because of the difficulty of measurement in experiments. In this paper, in order to get fundamental knowledge of them, 2-D unidirectional flow passing through circular cylinders was investigated using the Immersed Boundary Method with Physical Virtual Model, which satisfies with the boundary condition on the solid surface with Cartesian fluid grid. Results showed the pressure drop through circular cylinders reasonably agreed with experimental formulas. It was clear that the turbulent transition started from downstream to upstream and it was showed by the analysis of fluid force acting on each cylinder.

INTRODUCTION

Porous media flow phenomena can be widely observed in engineering field. Complexity of apertures of a porous media cause complicated flow inside and around it, and moreover, fluid forces which act on respective members of a porous media considerably vary in time and space. From the viewpoint of design of porous structures, for example, breakwater, gravel bed, spur dike and so on, it is important to estimate these complicated fluid motion and forces accurately. Booij et al. (1998) measured fluid velocities at some fixed points inside gravel bed with the laser-Doppler technique in order to clear the mechanism of sand transport by turbulent flow in gravel bed. However, it is very difficult to get instantaneous velocity information at all apertures from physical experiment due to the limitation of measurement technique.

The purpose of this study is to obtain the knowledge of fluid motion inside a porous media and of fluid forces act on members of a porous media by using numerical simulation. However, general porous media has a complex three dimensional apertures inside it and it is difficult to consider it first. Therefore, we tried to simulate the flow passing through circular cylinder array with different Reynolds numbers as the first attempt to understand the porous media flow. In numerical simulation of fluid motion, handling of the complex geometric solid boundaries in fluid is difficult because it is necessary to fit numerical fluid cell boundaries to solid boundaries. Immersed Boundary Method (IBM) originally presented by Peskin (1977) is simple simulation methods which can easily introduce the solid boundary conditions with normal orthogonal fluid cell. Recently, the validity and availability of the IBM have been presented by many researchers (Lima e Silva et al., 2003, Lee and Mizutani, 2007, Compregher et al., 2009).

In this study, we used this IBM technique for implementation of complex solid boundaries in numerical simulation. Furthermore, we could obtain the information of fluid force on each solid boundaries by using IBM and investigate the characteristics of fluid force on each cylinder.

MATHEMATICAL MODEL

Fundamental Equations

The main idea of the IBM is to use a regular Eulerian grid to simulate the fluid flow, together with Lagrangian points distributed over fluid-solid surface in calculation domain. A force field is evaluated at the Lagrangian points in order to no-slip boundary condition, and then distributed over the Eulerian nodes using a discretized Dirac delta function. Therefore, additional virtual force term to implement solid boundary should be added to the Navier-Stokes equations.

In this study, we assumed the incompressible and viscous fluid, therefore the following momentum and continuity

equations were used.

$$\rho\left[\frac{\partial\vec{V}}{\partial t}+(\vec{V}\cdot\nabla)\vec{V}\right]=-\nabla P+\mu\nabla^2\vec{V}+\vec{f} \quad (1)$$

$$\nabla\cdot\vec{V}=0 \quad (2)$$

where ρ and μ are density and viscosity of fluid respectively. $\vec{f}$ means additional (Eulerian) force source term in order to guarantee the no-slip boundary condition on the surface of solid wall. Additional force $\vec{f}$ acts only the fluid nearby the solid wall and is calculated the following equation.

$$\vec{f}=\int\vec{f}_k\delta(\vec{x}-\vec{x}_k)dx_k \quad (3)$$

where $\delta(\vec{x}-\vec{x}_k)$ is a Dirac delta function, $\vec{x}_k$ is a coordinate vector of Lagrangian points placed over the immersed boundary and $\vec{f}_k$ is a reactional force vector on the solid surface points. In order to calculate the distributed additional force $\vec{f}$, discretized Dirac delta function D_{ij} (distribution function) was used.

$$D_{ij}=\frac{f_1[(x_k-x_i)/\Delta x]f_1[(y_k-y_j)/\Delta y]}{\Delta x\Delta y} \quad (4)$$

$$f_1=\begin{cases}f_2(r), & if|r|<1\\ \frac{1}{2}-f_2(r), & if1<|r|<2\\ 0, & if2<|r|\end{cases} \quad (5)$$

$$f_2(r)=\frac{3-2|r|+\sqrt{1+4|r|-4|r|^2}}{8} \quad (6)$$

where r is a normalized distance between the Lagrangian point and fluid cell ($(x_k-x_i)/\Delta x$ or $(y_k-y_j)/\Delta x$), Δx is a fluid cell length. Eq.3 is able to be rewrited to the following equation by using Eq.4.

$$\vec{f}=\Sigma D_{ij}\vec{f}_k\Delta k^2 \quad (7)$$

where Δk is the distance between the Lagrangian points.

Physical Virtual Model

A variety of ways to calculate the additional force (Lagrangian force) $\vec{f}_k$ were presented (Goldstein et al.,1993, Fadlun et al., 2000). In this study, the Physical Virtual Model (PVM) presented by Silva et al. (2003) was used to calculate $\vec{f}_k$. The feature of PVM is the usage of Navie-Stokes equation to calculate the fluid force acting on solid surface as follows. which balances out the momentum equation, over the Lagrangian points. Therefore, $\vec{f}_k$ is evaluated by following Navier-Stokes equation.

$$\vec{f}_k=\rho\frac{\partial\vec{V}_k}{\partial t}+\rho(\vec{V}_k\cdot\nabla)\vec{V}_k-\mu\nabla^2\vec{V}_k+\nabla P_k \quad (8)$$

where $\vec{V}_k$ and P_k is a fluid velocity vector and pressure on Lagrangian solid surface points respectively. Actually, velocity vector on solid surface is zero, but $\vec{V}_k$ is a temporary velocity estimated from fluid velocity information around it by interpolation procedure and is not necessary zero. In order to calculate the first and second spatial derivatives of $\vec{V}_k$ and P_k in Eq. 4, second-order Lagrangian polynomial interpolation method was used.

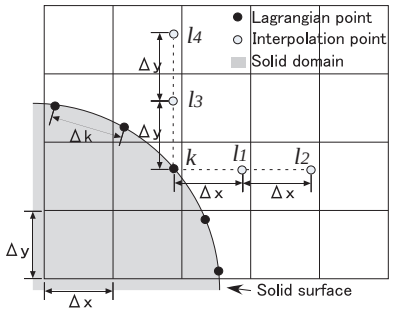

Figure 1. Definition of Lagrangian point k and auxiliary points l_1,l_2,l_3,l_4 for Lagrangian polynomial interpolation

$$\frac{\partial\phi_k}{\partial x}=\frac{(x_k-x_2)}{(x_1-x_2)(x_1-x_k)}\phi_1+\frac{(x_k-x_1)}{(x_2-x_1)(x_2-x_k)}\phi_2+\frac{(x_k-x_1)+(x_k-x_2)}{(x_k-x_1)(x_k-x_2)}\phi_k \quad (9)$$

$$\frac{\partial^2\phi_k}{\partial x^2}=\frac{2\phi_1}{(x_1-x_2)(x_1-x_k)}+\frac{2\phi_2}{(x_2-x_1)(x_2-x_k)}+\frac{2\phi_k}{(x_k-x_1)(x_k-x_2)} \quad (10)$$

where ϕ is generalized the fluid velocity and pressure. x_k is a x-coordinate of Lagrangian points, x_1 and x_2 are x-coordinates of auxiliary points which are Δx, $2\Delta x$ distant from x_k respectively toward the fluid, as shown in Fig.1. Velocity and pressure information at auxiliary points (for example, ϕ_1 and ϕ_2 in Eq. 5 and Eq. 6) and at Lagragian points (ϕ_k) are necessary for Lagrangian polynomial interpolation, and they were interpolated from neighboring fluid cell data. However, when ϕ_k was calculated, not only fluid cell but also internal solid cell data was used for interpolation exceptionally. In the same way, the derivatives in the y direction was obtained. The first term of Eq.8 was calculated by $(\vec{V}_{kb}-\vec{V}_k)/\Delta t$ using the moving velocity $\vec{V}_{kb}$ of the Lagrangian points, where Δt is the computational time step. In this study, we set the condition that cylinder array are fixed, therefore $\vec{V}_{kb}$ was assumed to be zero. After the caliculation of Lagrangian force $\vec{f}_k$ by using Eq.8 was finished, $\vec{f}_k$ was distributed over the neighboring fluid cell to meet the boundary condition.

Numerical Method

Eq. 1 and Eq. 2 are discretized using the second-order Adams-Bashforth method in time and the second-order finite central difference method in space. The fluid velocity and pressure coupling is solved with SMAC scheme. This scheme is described as follows:

$$\frac{\bar{u}_i^n - u_i^n}{\Delta t} = -\frac{1}{\rho}\frac{\partial P^n}{\partial x_i} + \frac{3}{2}\{(ADV_i^n + VIS_i^n + f_i^n) - (ADV_i^{n-1} + VIS_i^{n-1} + f_i^{n-1})\} \quad (11)$$

$$\frac{\partial^2 \phi^n}{\partial x_i \partial x_i} = \frac{\rho}{\Delta t}\frac{\partial \bar{u}_i^n}{\partial x_i} \quad (12)$$

$$P^{n+1} = P^n + \phi^n \quad (13)$$

$$u_i^{n+1} = \bar{u}_i^n - \frac{\rho}{\Delta t}\frac{\partial \phi^n}{\partial x_i} \quad (14)$$

where,

$$ADV = \frac{\partial (u_i u_j)}{\partial x_j} \quad (15)$$

$$VIS = \frac{\mu}{\rho}\frac{\partial^2 u_i}{\partial x_j \partial x_j} \quad (16)$$

where $\bar{u}_i$ is the temporary velocity, ϕ is the scalar value to correct pressure and n is the sub-step indices. One cycle of the numerical procedure is as follows:

1. Calculate the Lagrangian force $\vec{f}_k$ acts on solid surface, using Eq.8.
2. Distribute $\vec{f}_k$ to the fluid cell nearby solid surface and calculate the additional force f_i, acts on fluid parcel using Eq. 10.
3. Calculate the temporary fluid velocity $\bar{u}_i$, using Eq.11.
4. Solve the poisson Eq.12 for the pressure correction, using MICCG method.
5. Update the fluid velocity and pressure using Eqs.13 and 14.

THE FLOW PASSING THROUGH A SINGLE CIRCULAR CYLINDER

In order to validate our numerical model, fluid motion and fluid force around a circular cylinder in unidirectional flow was calculated for different Reynolds number conditions. Reynolds number was defined as $Re = U_{in}d/\nu$, where ν is a kinematic viscocity coefficient. Results were compared with physical and numerical experiments results in previous studies.

Calculation Conditions

A single circular cylider was placed at the center of computational domain $30d$ in length and $30d$ in width, where d is the cylinder diameter (Fig.2). Before starting main calculation, several preliminary experiments were conducted for the check of boundary condition effect, and we decided this domain finally. Constant unidirectional flow condition (U_{in} : approaching velocity) was specified at inflow boundary ($x = 0$) and Sommerfeld radiation condition was imposed at outflow boundary ($x = 30d$). On the lateral boundary boundaries, free-slip (Neumann) condition was set.

In IBM simulation, uniform length fluid cells were able to be used, but the accuracy itself was depending on the resolution of fluid cells. For example, preliminary simulations with different resolution $d/\Delta x$ (Δx is a fluid cell length) showed that the drag coefficient C_D($C_D = 2F_D/(\rho U_{in}^2 d)$ was changed depending on $d/\Delta x$, where F_D is a gross Lagrangian force in x-direction. Lima e Silva et al. (2003) decided the appropriate resolution as $\Delta k/\Delta x < 0.9$, where Δk is distance between the Lagrangian points. Based on these knowledge, our numerical experiments were conducted for different Reynolds numbers (Re=10∼1000) under the consition that $d/\Delta x = 10$ and $\Delta k/\Delta x = 0.523$ after sensitivity analysis of computational resolution.

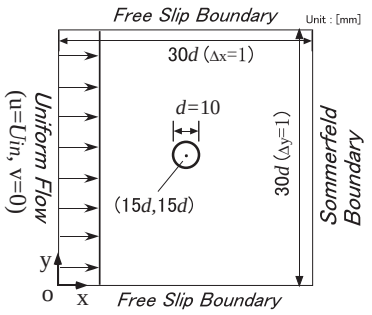

Figure 2. Analysis domain and boundary conditions in case that the flow passing through a single circular cylinder

Simulation Results For The Flow Passing Through A Single Circular Cylinder

Fig.3 shows the distribution of instantaneous fluid velocity vector and dimensionless vorticity $\omega* = (\partial v/\partial x - \partial u/\partial y)/(U_{in}/d)$ of the flow passing through a single cylinder when Re is 40 and 50 respectively. The flow was symmetric in Re = 40, but turned to assymmetric and instability flow in Re = 50. This feature was reasonable when comparing to previous studies results, for example, Williamson (1996) presented the Karman vortex street could be seen over Re = 47.

The relationship between the Reynolds number Re and the drag coefficient C_d is shown in Fig.4. It is clear that our numerical simulations were good agreement with past physical experiment results presented by Schlichting et al. (???) and Wieselsberger (1922) and numerical experiment results (Re = 10∼300) conducted by Silva et al. (2003). And it means our model had a good performance to simulate the flow around a single cylinder. However, only one case in Re = 1000, calculated drag coefficient was different to that of physical experiment results. As the reason of this difference, it is able to cite the development of three dimensional characteristics of the flow. For example, Williamson (1996) and Maruoka et al. (1998) pointed out the fact that the fluid force acting on a cylinder calculated from two-dimensional simulation results exceeded that of observation value when the Reynolds number Re is around 1000 for comparing three dimensional simulation results. Our numerical result didn't deviate from these previous knowledge.

Next, the relationship between the Strouhal number $St = fd/U_{in}$, which is a dimensionless frequency of vortex shedding f, and the Reynolds number Re is shown in Fig.5. It looks like the Storouhal number approached to 0.2 with the in-

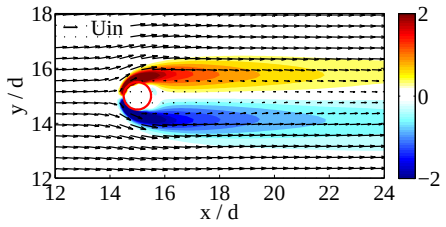

(a) $Re = 40$

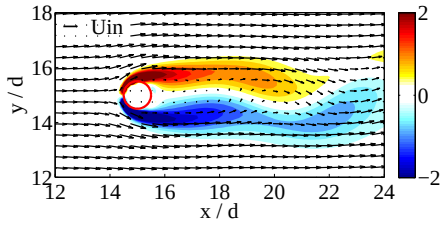

(b) $Re = 50$

Figure 3. Fluid velocity vector and vorticity distribution in Re = 40 (steady flow) and Re = 50 (unsteady flow)

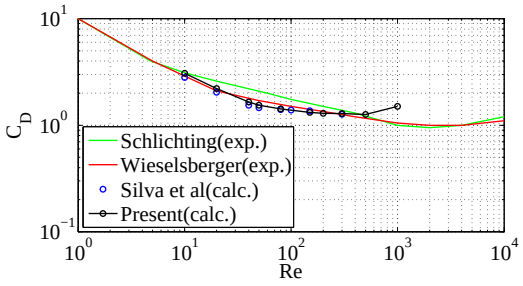

Figure 4. Relationship between drag coefficient C_D acting on a cylinder and Reynolds number Re.

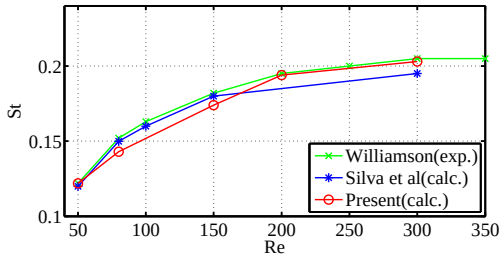

Figure 5. Relationship between Strouhal number St and Reynolds number Re

creaseing the Reynolds number. Our results were good agreement with previous physical experiment results presented by Williamson (1996) and numerical experiment results presented by Lima e Silva et al. (2003).

As discussed above, our numerical model performance to simulate the flow passing through a single cylinder was validated for comparing to previous physical and numerical simulation results.

UNIDIRECTIONAL FLOW PASSING THROUGH CIRCULAR CYLINDER ARRAY

The simulation results of two-dimensional flow passing through circular cylinder array settled in pipe were shown in this section. Our results were compared to previous physical experimant results with the famous relationship between macroscopic flow velocity and pressure drop.

Calculation Conditions

The detail of computational domain and boundary condition are shown in Fig.6. The computational domain was $50d$ in length and $8.3d$ in width, where d is a circular cylinder diameter d=12mm. 50 Circular cylinders were staggered from x=$8.3d$ to x=$14.4d$ and the distance between their centroids were D=20mm, and the length of the wake region behind cylinder array was $27.3d$. The porosity of cylinder array ε was 0.675. A steady two-dimensional poiseuille velocity profile was specified at $x = 0$ as inflow boundary and Sommerfeld radiation condition was imposed at x=$50d$ as outflow boundary. Then, no-slip conditions were set at the lateral boundary boundaries. The resolution was decided $d/\Delta x = 12.0$, and this value was slightly finer than that of the preliminary simulation of the flow passing around a single cylinder. The Reynolds number was defined as $Re = Ud/\nu(1-\varepsilon)$, where U is a cross-sectional mean velocity. Simulations were conducted for different Reynolds number varied from 5 to 1000.

Simulation Results For The Flow Passing Through Circular Cylinder Array

First, Fig.7 shows the distribution of instantaneous dimensionless vorticity ω^* of the flow passing through circular cylinder array for Re = 98, 245 and 490. When the Reynolds number was small, Re = 98, positive and negative vorticities were distributed symmetrically to dominant flow direction nearby each cylinder, and their distribution pattern were almost same in all apertures except the close place to the pipe wall (the wall effect was so small where about $1D$ away from pipe wall). And it is clear that the laminar rotational jet flow was observed behind cylinder array. Next, for the case Re = 245, vorticitie behind each cylinders became large and spread to downstream, but symmetric distribution pattern was still maintained. On the other hand, the laminar flow behind cylinder array was broken and turned to unsteady flow. Jet flows ejected each apertures were mixed after flowing down about $2\sim3d$, and after that, regular vortex street, such as Karman vortex, was observed. Then, in enough large Reynolds number condition, Re = 490, it is interesting that vorticities at the upstream region ($0 < x/d < 5$) were still distributed symmetrically and were steady, but vorticities at the downstream region ($5 < x/d < 15$) were distributed irregularly and were unsteady. Moreover, large and small scale vorticities was generated irregularly in the wake region. Our numerical model didn't include turbulence model, but results showed complicated and unsteady flow was generated in apertures for relatively low Reynolds number condition. This feature indicates the relation to the knowledge of macroscopic pressure drop law depending on the square of velocity for low Reynolds number. Furthermore, the knowledge that the unsteady flow was developed at the downstream region first, and it spread toward to upstream region was interesting. Next, the accuracy concern

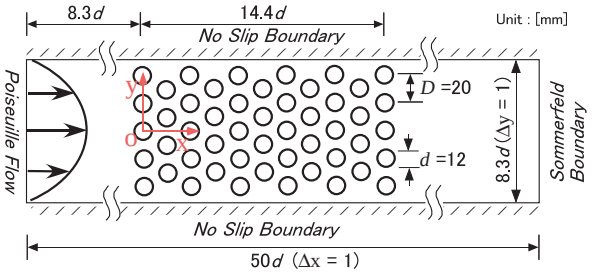

Figure 6. 50 cylinders in zigzag alignment in calculation domain and boundary condition

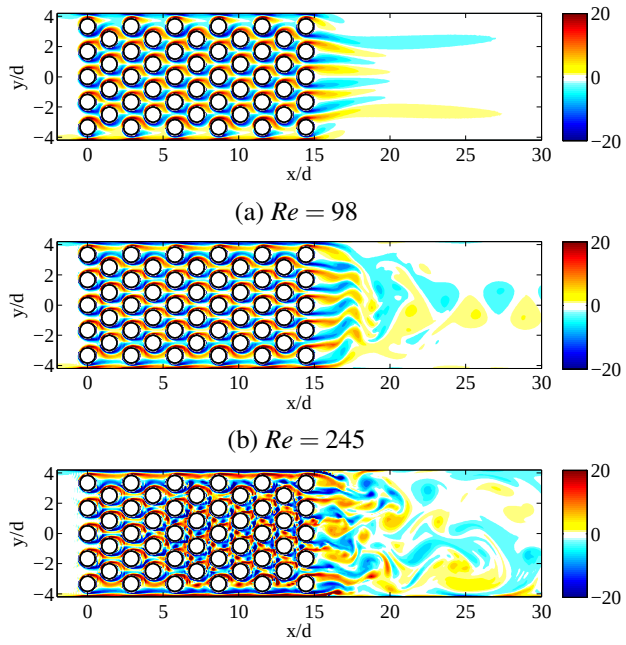

(a) $Re = 98$

(b) $Re = 245$

(c) $Re = 490$

Figure 7. Distribution of dimensionless vorticity around circular cylinders

with the macroscopic pressure drop law was investigated. The pressure drop ΔP when fluid flow passing through a porous media was able to estimate using the following famous experimental formula (Ergun, 1952):

$$\frac{\Delta P}{\ell} = 150\frac{(1-\varepsilon)^2}{\varepsilon^3}\frac{\mu U}{D_p^2} + 1.75\frac{(1-\varepsilon)}{\varepsilon^3}\frac{\rho U^2}{D_p} \qquad (17)$$

where ℓ is the length of porous media, D_p is effective diameter of components of porous media. Assuming d equaled to D_p, an experimental pressure drop can be calculated using Eq.17. Naturally, ΔP was able to be calculated from our numerical simulation results. In order to compare these two pressure drops, the another nondimension value, friction factor C_f, was

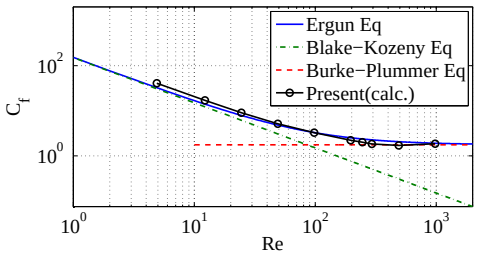

Figure 8. Dimensionless pressure drop C_f and Reynolds number Re

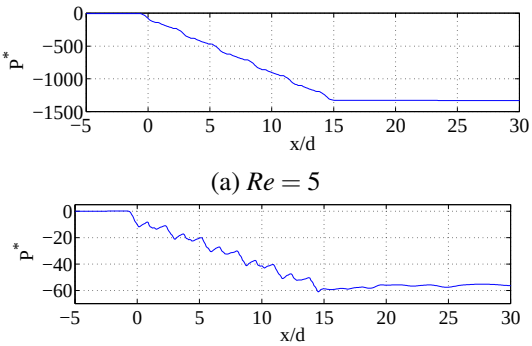

(a) $Re = 5$

(b) $Re = 490$

Figure 9. Cross-sectional averaged pressure distribution for the flow passing through cylinder array

calculated using the following equation:

$$C_f = \frac{\Delta P}{\ell}\frac{D_p}{\rho U^2}\frac{\varepsilon^3}{(1-\varepsilon)} \qquad (18)$$

The relationship between C_f and Reynolds number Re is shown in Fig.8. Here, Blake-Kozeny equation is an experimental equation for the laminar porous media flow, and Burke-Plummer equation is an experimental equation for turbulent porous media flow respectively. Our numerical simulation results were good agreement with the estimation value by Ergun's experimental equation for Re = 5 $\sim$ 1000. Fig.9 shows dimensionless cross-sectional average pressure $P^* = (< P > -P_{in})/(\rho U^2 d/2)$ distribution for Re = 5 and 490, where P_{in} is the pressure at the inlet of the cylinder array. Monotonically P^* was decreasing with the fluid passing through cylinder array in both cases. However, the fluctuation of P^* was larger in the case of Re = 490 than that of in the case of Re = 5. Finally, the characteristics of fluid forces acted on each cylinder was investigated. Fig.10 shows the time variation of fluid velocity vectors and dimensionless fluid force vectors $F^*(C_D, C_L)$ acted on each circular cylinder for Re = 490. As shown in these figure, complicated fluid motion nearby each cylinder caused difference of fluid force direction and their magnitude, and they were not uniform and not steady. However, its extent depended on the distance from the inlet of cylinder array, the direction of fluid forces near the inlet were not so changed, on the other hand, that of near

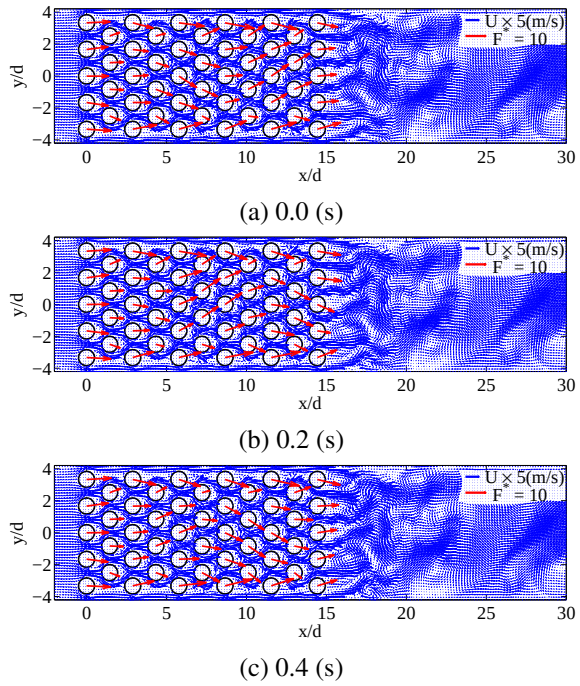

(a) 0.0 (s)

(b) 0.2 (s)

(c) 0.4 (s)

Figure 10. Time variation of fluid motion and force acted on each circular cylinder for Re = 490

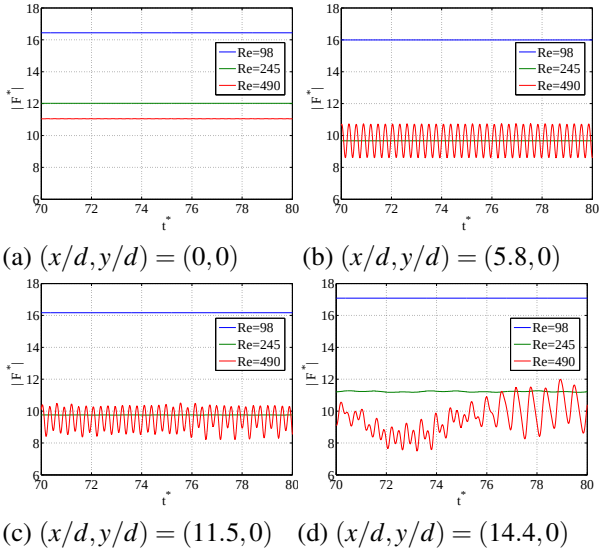

(a) $(x/d, y/d) = (0, 0)$ (b) $(x/d, y/d) = (5.8, 0)$

(c) $(x/d, y/d) = (11.5, 0)$ (d) $(x/d, y/d) = (14.4, 0)$

Figure 11. Time-series of fluid force acted on each circular cylinder for defferent Reynolds number

the outlet were varied significantly. This feature indicates the fact that the rear components of porous media can be moved or broken more easily than the front parts of it. Fig.11 shows that time series of the magnitude of fluid forces acted on representative cylinders placed on centeral axis for different Reynolds number Re = 98, 245 and 490. Each cylinder coordinate of centroid was $(x/d, y/d)$ = (0, 0), (5.8, 0), (11.5, 0), (14.4, 0) in order of distance from inlet of cylinder array respectively. First, in the case of Re = 98, steady fluid force acted on every cylinder, but their magnitude were different. The force acted on lead cylinder (a) was larger than that of inner cylinders (b) and (d), on the other hand, the force acted on terminal cylinder (d) was larger than that of lead cylinder. Terminal cylinder was effected by the wake flow behind cylinder array. Secondly, in the case of Re = 245, the nondimensional fluid forces were smaller than that of Re = 98 at every cylinder, and it was similar that the fluid force acted on lead cylinder was larger than that of inner cylinders. However, the force acted on terminal cylinder was smaller than that of lead cylinder, and slightly fluctuated. Finally, in the case of Re = 490, inner cylinders also recieved unsteady forces, but the force acted on lead cylinder was still steady. Unsteadiness of fluid forces became large with the distance from inlet of cylinder array, and that of terminal cylinder had clear long-period component. Moreover, time average force acted on terminal cylinder was almost same to that of inner cylinders.

CONCLUSIONS

The numerical simulation model which can easily treat the flow including complex solid boundary was constructed using Immersed Boundary Method. In order to validate our model, the flow passing around a single cylinder was simulated and it is cleared that simulated results were good agreement with previous physical and numerical experiments results for comparing the beginning of the unsteadiness of wake flow, and the drag coefficient and the Strouhal number variation for different Reynolds number. Reproducibility of the relationship between pressure drop and the Reynolds number was fine and it is clear that the cross-sectioal average pressure P^* decreased monotonically during the flow passing through cylinder array. However, the fluctuation of P^* became more larger with the increase of the Reynolds number. Laminar flow in cylinder array was turned to unsteady flow in relatively low Rynolds number and the unsteady flow was developed at the downstream region first, then it spread toward to upstream region. Complicated fluid motion nearby each cylinder caused difference of fluid force direction and their magnitude, and they were not uniform in cylinder array and they were not steady especially in downstream region. The direction of fluid forces near the inlet were not so changed, on the other hand, that of near the outlet were varied significantly. The force acted on lead cylinder was larger than that of inner cylinders, and the force acted on terminal cylinder was larger than that of lead cylinder in laminar flow regime. Unsteadiness of the fluid force acted on each cylinder became large with the increase of Reynolds number and with the distance from the inlet of cylinder array. Moreover, the force acted on terminal cylinder approached to that of inner cylinders. It is important to deal with these features cleared from microscopic numerical simulation to apply to macroscopic analysis in the next stage.

Acknowledgements

The present study was supported by Grant-in-Aid for Young Scientists (B) (23760460) and for Scientific Research (C) (22560521).

SAMPLE REFERENCES

Booij, R., Uijttewaal, W. S. J., Os, P., Fontijn, H. L., and Battjes, J. A., 1998, "The Influence of Pressure Fluctuations on the Flow Between Armour Elements", Proceedings 26th International Conference On Coastal Engineering, pp. 1898-1905.

Campregher, R., Militzer, J., Mansur, S. S., and Silveira-Neto, A., 2009, "Computations of the Flow Past a Still Sphere at Moderate Reynolds Numbers Using an Immersed Boundary Method", J. of the Braz. Soc. of Mech. Sci.& Eng., Vol. 31, No. 4, pp. 344-352.

Ergun, S., 1952, "Fluid Flow through Packed Columns", Chemical Engineering Progress, Vol. 48, No. 2, pp. 89-94.

Lee, K., and Mizutani, N., 2007, "Numerical Wave Flume with Immersed Boundary Method and its Applicability in Wave Field Simulation around a Horizontal Circular Cylinder, JSCE Annual Journal of Coastal Engineering, Vol. 54, pp. 821-825.

Lima e Silva, A. L. F., Silveira-Neto, A., and Damasceno, J. J. R., 2003, "Numerical Simulation of Two-Dimensional Flows over a Circular Cylinder using the Immersed Boundary Mehod", Journal of Computational Physics, Vol. 189, pp. 351-370.

Maruoka, A., Ohta, S., Hirano, H., and Kawahara, M., 1998, "Two and Three Dimensional Numerical Flow Analysis around a Circular Cylinder over Wide Range of the Reynolds Numbers", Journal of Structural Mechanics and Earthquake Engineering, No. 591, pp. 139-150.

Peskin, C. S., 1977, "Numerical Analysis of Blood Flow in the Heart", Journal of Computational Physics, Vol. 25, No. 3, pp. 220-252.

Wieselsberger, C., 1922, "New Data on the Laws of Fluid Resistance", NACA TN, No. 84.

Williamson, C. H. K., 1996, "Vortex Dynamics in the Cylinder Wake", Annual Review of Fluid Mechanics, Vol. 28, pp. 477-539.